

Sub-diffusion flow velocimetry with number fluctuation optical coherence tomography

Cheishvili, K.; Kalkman, J.

DOI

[10.1364/OE.474279](https://doi.org/10.1364/OE.474279)

Publication date

2023

Document Version

Final published version

Published in

Optics Express

Citation (APA)

Cheishvili, K., & Kalkman, J. (2023). Sub-diffusion flow velocimetry with number fluctuation optical coherence tomography. *Optics Express*, 31(3), 3755-3773. <https://doi.org/10.1364/OE.474279>

Important note

To cite this publication, please use the final published version (if applicable).
Please check the document version above.

Copyright

Other than for strictly personal use, it is not permitted to download, forward or distribute the text or part of it, without the consent of the author(s) and/or copyright holder(s), unless the work is under an open content license such as Creative Commons.

Takedown policy

Please contact us and provide details if you believe this document breaches copyrights.
We will remove access to the work immediately and investigate your claim.



Sub-diffusion flow velocimetry with number fluctuation optical coherence tomography

KONSTANTINE CHEISHVILI*  AND JEROEN KALKMAN 

Department of Imaging Physics, Delft University of Technology, Lorentzweg 1, 2628 CJ Delft, Netherlands
*k.cheishvili@tudelft.nl

Abstract: We have implemented number fluctuation dynamic light scattering optical coherence tomography (OCT) for measuring extremely slow, sub-diffusion flows of dilute particle suspensions using the second-order autocovariance function. Our method has a lower minimum measurable velocity than conventional correlation-based OCT or phase-resolved Doppler OCT, as the velocity estimation is not affected by the particle diffusion. Similar to non-dilute correlation-based OCT, our technique works for any Doppler angle. With our analysis we can quantitatively determine the concentration of particles under flow. Finally, we demonstrate 2D sub-diffusion flow imaging with a scanning OCT system at high rate by performing number fluctuation correlation analysis on subsequent B-scans.

© 2023 Optica Publishing Group under the terms of the [Optica Open Access Publishing Agreement](#)

1. Introduction

Dynamic light scattering optical coherence tomography (DLS-OCT) relies on the measurement of fluctuations of scattered light and coherence gating to obtain simultaneous depth-resolved information about diffusive and translational motion of particles. This information is extracted from the temporal autocorrelation of the OCT signal for every voxel in depth. Initially, DLS-OCT was used for quantitative diffusion imaging [1] and quantitative flow imaging of non-dilute particle suspensions [2–4].

DLS-OCT has the advantage over the phase resolved Doppler OCT that a flow can be measured for zero Doppler angle. However, for both methods the velocity sensitivity is limited by signal-to-noise ratio (SNR) [5] and the Brownian motion of the flowing particles [2,6]. In that case, the Doppler phase shifts and the scattered light intensity fluctuations are small, are buried in the noise, or are overwhelmed by the phase/intensity changes caused by Brownian motion. Hence, it is challenging to measure sub-diffusion transverse flow rates. However, for very dilute suspensions particle motion gives rise to additional fluctuations in the scattered intensity at longer time scales compared to particle diffusion [7,8] and enables measurement of a sub-diffusion flow velocity.

In this work we utilize particle number fluctuations of dilute suspensions in DLS-OCT to improve the minimum measurable velocity of omnidirectional flows. We combine and extend the existing theoretical models for the normalized second-order OCT signal autocovariance and incorporate number fluctuations into them. We show that when using number fluctuations, the minimum measurable velocity of DLS-OCT is freed from the constraint imposed by diffusion. Hence, lower flow velocities can be measured compared to conventional non-dilute DLS-OCT or Doppler OCT.

2. Theory

The typical geometry for point scanning OCT flow measurements is visualized in Fig. 1. The propagation of the optical beam is along the z direction. The flow is in a channel oriented at an angle α with respect to the x - y plane. This angle can, due to refraction of the light, be different from the orientation of the flow direction at angle θ . In general, we assume the flow to be laminar with transverse, $v_r(z)$, and axial, $v_z(z)$, velocity components as a function of depth. Given a total

flow $v_0(z)$, the flow components are expressed as $v_r(z) = v_0(z) \cos \theta$ and $v_z(z) = v_0(z) \sin \theta$. The OCT beam is a Gaussian beam characterized by a waist w_0 in focus, and the local beam waist $w(z)$ at location z along the optical axis. The beam waist is defined as a distance from the beam center where the beam intensity is e^{-2} of its maximum value. The combination of the Gaussian-shaped lateral intensity and the axial coherence function gives the OCT point spread function (PSF) in the z and r -directions

$$I(r, z) = e^{-\frac{4r^2}{w^2(z)}} e^{-\frac{2z^2}{w_z^2}}, \quad (1)$$

where r is the radial distance from the beam center, z is the axial position, and w_z is the coherence function waist (e^{-2} intensity distance) in the sample. The additional factor 2 in the radial PSF function is due to coupling efficiency of the scattered light in a confocal setup [2,9]. For the Gaussian source spectrum with a wavenumber standard deviation σ_k and sample refractive index n , the coherence function waist is given by $w_z^{-1} = \sqrt{2}\sigma_k n$.

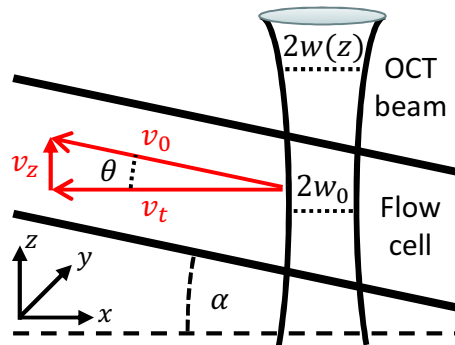


Fig. 1. Geometry of the OCT sample arm and the fluid flow.

In this work we discuss three different techniques for performing quantitative OCT flow measurements, namely

- Doppler OCT
- Non-dilute DLS-OCT
- Number fluctuation DLS-OCT

where the last method is the new method developed by us.

2.1. Doppler OCT

The most commonly used method for measuring the axial flow velocity is phase-resolved Doppler OCT. The Doppler effect gives a frequency shift to the light scattered from a particle undergoing axial motion. The Doppler frequency shift of the spectral OCT signal is equivalent to a phase change of the spatial OCT signal, $\Delta\phi(z)$. From the phase change the axial depth-resolved velocity $v_z(z)$ is determined using [10]

$$v_z(z) = \frac{2\pi f_D(z)}{q} = \frac{\Delta\phi(z)}{q\Delta t}, \quad (2)$$

where f_D is the Doppler frequency shift of the scattered light, Δt is the sampling time, and $q = 2nk_0$ is the scattering wavenumber for the OCT backscattering probe configuration with the medium refractive index n and the vacuum wavenumber k_0 . The total and axial flow velocities are

related through $v_0(z) = v_z(z)/\sin \theta$. For a shot-noise limited OCT system, the smallest observable change in the phase measurement, $\delta\phi_{\text{sens}}$, can be obtained using [5,11,12]:

$$\delta\phi_{\text{sens}} = \frac{2}{\pi} \int_0^{\pi/2} \tan^{-1} \left(\sqrt{\frac{I_n}{I_s}} \sin \phi_{\text{rand}} \right) d\phi_{\text{rand}} \approx \frac{2}{\pi\sqrt{\text{SNR}}}, \quad (3)$$

where ϕ_{rand} is the random phase of the shot noise with uniform probability distribution over the range from 0 to 2π and $\text{SNR} = \frac{\langle I_s \rangle}{\langle I_n \rangle}$ is the measurement signal-to-noise ratio with I_s and I_n being the OCT signal and noise intensities, respectively. The minimum axial velocity that for a given signal-to-noise ratio can be estimated is obtained by replacing $\Delta\phi$ in Eq. (2) with $\delta\phi_{\text{sens}}$ from Eq. (3), which results in

$$v_{z_{\text{min,SNR}}} = \frac{2^{3/2}}{\pi q \Delta t \sqrt{\text{SNR}} \cdot M}, \quad (4)$$

where the additional factor of $\sqrt{2}$ in the numerator arises because the estimated velocity is proportional to the numerical difference between the measured phase and a reference phase [5]. The variable M in the denominator is the number of statistically independent phase change measurements for calculating the axial velocity. Averaging increases the flow sensitivity by a factor of \sqrt{M} .

The axial velocity sensitivity of Doppler OCT is further limited by the particle diffusion [6,13,14]. Particle diffusion causes frequency broadening of the Doppler shifted scattered light resulting in a particle diffusion broadened Lorentzian [15,16]. For a single wavelength heterodyne system the full width at half maximum (FWHM) of the particle diffusion broadened Lorentzian is Dq^2/π , where D is the particle diffusion coefficient. However, in Fourier domain OCT the Doppler phase is calculated by multiplying/dividing intensities from different pixels on the camera, resulting in a twice as big FWHM, i.e., $\text{FWHM} = 2Dq^2/\pi$ [1]. Using this FWHM as a measure of the frequency sensitivity together with Eq. (2), we obtain the minimum measurable axial velocity in the presence of the particle diffusion:

$$v_{z_{\text{min,Diff}}} = \frac{4Dq}{\sqrt{M}}. \quad (5)$$

Assuming that both noise and diffusion are independent and not correlated, the overall axial velocity sensitivity can be expressed as

$$v_{z_{\text{min}}} = \sqrt{v_{z_{\text{min,SNR}}}^2 + v_{z_{\text{min,Diff}}}^2}, \quad (6)$$

with the total velocity sensitivity given by $v_{0_{\text{min}}} = v_{z_{\text{min}}}/\sin \theta$.

2.2. Non-dilute DLS-OCT

Non-dilute DLS-OCT is based on light intensity fluctuations and is sensitive to both axial and transverse flows. For a Gaussian illuminating beam and Gaussian-shaped spectral envelope, the normalized depth-dependent autocovariance of the OCT complex signal in a backscattering geometry, including the effect of SNR, is given by [2,3,17–19]

$$g_1(z, \tau) = \frac{1}{1 + \frac{1}{\text{SNR}(z)}} e^{iqv_z(z)\tau} e^{-Dq^2\tau} e^{-\frac{v_0^2(z) \sin^2 \theta \tau^2}{2w_z^2}} e^{-\frac{v_0^2(z) \cos^2 \theta \tau^2}{w_0^2}}, \quad (7)$$

where τ is the autocovariance time lag. In Eq. (7) the effect of a gradient of the axial velocity on the autocovariance function is neglected. Note that the transverse decorrelation in Eq. (7) only depends on the in-focus beam radius w_0 [8,18,20]. The decay rate of the OCT signal intensity or

magnitude is a factor two higher [1,18] than the field decorrelation and can be expressed with the normalized second-order autocovariance [15,16]

$$g_2(z, \tau) = |g_1(z, \tau)|^2 = \frac{1}{\left(1 + \frac{1}{\text{SNR}(z)}\right)^2} e^{-2Dq^2\tau} e^{-\frac{v_0^2(z)\sin^2\theta\tau^2}{w_z^2}} e^{-\frac{2v_0^2(z)\cos^2\theta\tau^2}{w_0^2}}, \quad (8)$$

where we have used the Siegert relation (for a normalized second-order autocovariance the Siegert relation does not contain a constant offset). In deriving $g_2(z, \tau)$ we have assumed that the average number of particles in the scattering volume, N , is sufficiently large ($N \gtrsim 100$) [7,8,16]. This ensures that the particle probability distribution in the scattering volume and the scattered light fluctuations follow Gaussian statistics. This requirement is almost always satisfied for typical OCT resolutions and particle concentrations. Deviation from the Gaussian approximation requires extremely dilute samples and/or very small scattering volumes that can be achieved with extremely high spatial resolution. In this work we focus on the normalized second-order autocovariance function $g_2(z, \tau)$ for flow measurements as it does not depend on phase, is easier to implement, and can also be implemented in phase-unstable OCT systems.

Diffusion and flow decay functions multiply each other in $g_2(z, \tau)$. Therefore, to accurately determine the flow velocity, the flow decay must dominate over the diffusion decay. This depends on the dynamic time constants τ_{v_0} and τ_D (e^{-1} decay times) of flow and diffusion decorrelations, respectively. Hence, for the flow decay to dominate we require that $\tau_{v_0} \ll \tau_D$ [2], where

$$\tau_D = (2Dq^2)^{-1}, \quad (9)$$

and

$$\tau_{v_0} = \left(v_0 \sqrt{\frac{\sin^2\theta}{w_z^2} + \frac{2\cos^2\theta}{w^2(z)}} \right)^{-1}. \quad (10)$$

By combining and inverting Eq. (9,10) we obtain the relation

$$v_0 \sqrt{\frac{\sin^2\theta}{w_z^2} + \frac{2\cos^2\theta}{w_0^2}} \gg 2Dq^2. \quad (11)$$

In the limiting case when both decays are equally strong, the minimum measurable diffusion-limited velocity for the normalized second-order autocovariance function is

$$v_{0,\text{min,Diff}} = 2Dq^2 \left[\frac{\sin^2\theta}{w_z^2} + \frac{2\cos^2\theta}{w_0^2} \right]^{-1/2}. \quad (12)$$

A finite signal-to-noise ratio further limits the minimum velocity that can be determined using intensity-based non-dilute DLS-OCT. The SNR-limited smallest observable relative change in the intensity can be obtained using [5]

$$\frac{\delta I_{\text{sens}}}{I_s} = \frac{2}{\pi\sqrt{M}} \int_0^{\pi/2} \frac{I_n}{I_s} \cos^2\phi_{\text{rand}} d\phi_{\text{rand}} = \frac{1}{2\text{SNR}\sqrt{M}}, \quad (13)$$

where the sensitivity improvement by a factor of \sqrt{M} comes from recording M statistically independent observations, which we assume has the same effect for both non-dilute DLS-OCT and Doppler OCT methods.

To estimate the limit imposed by the SNR on the DLS-OCT flow sensitivity the change of the intensity of light scattered by particles is considered. The amount of scattered light varies as the

particles undergo bulk motion with respect to the illuminating beam described by Eq. (1). The expected relative intensity change in a single time step due to transverse and axial particle motion can be estimated by moving the particle within the corresponding PSF by a distance traveled during the acquisition time Δt . Calculation of the relative intensity change requires splitting the analysis in a transverse and axial part and averaging over all possible particle locations. The expected relative intensity changes are

$$\frac{\delta I_t}{I_s} = \frac{\int_{-\infty}^{\infty} \left| e^{-\frac{4r^2}{w^2(z)}} - e^{-\frac{4(r+v_0\Delta t \cos \theta)^2}{w^2(z)}} \right| dr}{\int_{-\infty}^{\infty} e^{-\frac{4r^2}{w^2(z)}} dr} = \operatorname{erf} \left(\frac{2v_0\Delta t \cos \theta}{w(z)} \right) \quad (14)$$

and

$$\frac{\delta I_z}{I_s} = \frac{\int_{-\infty}^{\infty} \left| e^{-\frac{2z^2}{w_z^2}} - e^{-\frac{2(z+v_0\Delta t \sin \theta)^2}{w_z^2}} \right| dz}{\int_{-\infty}^{\infty} e^{-\frac{2z^2}{w_z^2}} dz} = \operatorname{erf} \left(\frac{\sqrt{2}v_0\Delta t \sin \theta}{w_z} \right) \quad (15)$$

for transverse and axial particle motions, respectively. Here we have neglected prefactors of exponential functions as they are identical both for numerator and denominator and cancel out. Finally, the expected relative intensity change due to a particle displacement with velocity v_0 after time step Δt can be determined by combining transverse and axial parts into

$$\frac{\delta I_0}{I_s} = \sqrt{\left(\frac{\delta I_t}{I_s} \right)^2 + \left(\frac{\delta I_z}{I_s} \right)^2}. \quad (16)$$

In the autocorrelation analysis, the particle flow limit is determined by the flow for which the relative intensity change is larger than or equal to, the smallest observable relative intensity change. Therefore, the SNR-limited minimum measurable velocity can be determined by solving the equation

$$\frac{\delta I_0}{I_s} = \frac{\delta I_{\text{sens}}}{I_s} \quad (17)$$

or equivalently

$$\sqrt{\operatorname{erf} \left(\frac{2v_{0,\text{min},\text{SNR}}\Delta t \cos \theta}{w(z)} \right)^2 + \operatorname{erf} \left(\frac{\sqrt{2}v_{0,\text{min},\text{SNR}}\Delta t \sin \theta}{w_z} \right)^2} = \frac{1}{2\text{SNR}\sqrt{M}}, \quad (18)$$

and finding the unknown $v_{0,\text{min},\text{SNR}}$. The minimum total velocity limit is then

$$v_{0,\text{min}} = \sqrt{v_{0,\text{min},\text{SNR}}^2 + v_{0,\text{min},\text{Diff}}^2}. \quad (19)$$

Note that this is a rough estimate using only a single change in the scattered light intensity and assuming a factor \sqrt{M} improvement for M observations. In DLS-OCT the determination of the flow is performed using a fit to the normalized autocovariance function requiring a multitude of points that could further affect the actual velocity sensitivity. In addition, the sampling time Δt should be smaller than the transit time affecting the effective number of points that could be used for the fit.

2.3. Number fluctuation DLS-OCT

Chowdhury et al. [7] suggested that in the limit of low number of particles in the scattering volume, the dilute case with $N \ll 100$, the DLS-OCT relations for the normalized second-order autocovariance function do not apply any more as they are derived for an infinite number of particles, i.e., $g_2(z, \tau) \neq |g_1(z, \tau)|^2$. For a low number of particles in the scattering volume, additional correlations appear in the intensity due to fluctuations in the total number of scatterers in the detected volume [21]. In this low particle number limit, the normalized second-order autocovariance function containing the effect of number fluctuations is given by

$$g_2(z, \tau) = \underbrace{|g_1(z, \tau)|^2}_{\text{Gaussian term}} + \underbrace{\langle \delta N(0)\delta N(\tau) \rangle}_{\text{number fluctuation term}}, \quad (20)$$

where the first term is known as the Gaussian, non-dilute, or coherent term, while the second term is known as the non-Gaussian, number fluctuation, dilute, number density, or incoherent term [7,8,15,16]. Following the derivation of Chowdhury et al. [7] and Taylor and Sorensen [8], incorporating the effects of SNR [19] and a light beam with a Gaussian lateral and axial PSF, the total normalized second-order autocovariance function $g_2(z, \tau)$ can be obtained as

$$g_2(z, \tau) = \frac{1}{\left(1 + \frac{1}{\text{SNR}(z)}\right)^2} \frac{2^{3/2}\langle N \rangle}{2^{3/2}\langle N \rangle + 1} \left[e^{-2Dq^2\tau} e^{-\frac{w_0^2(z)\sin^2\theta\tau^2}{w_z^2}} e^{-\frac{2w_0^2(z)\cos^2\theta\tau^2}{w_0^2}} \right. \\ \left. + \frac{1}{2^{3/2}\langle N \rangle} e^{-\frac{w_0^2(z)\sin^2\theta\tau^2}{w_z^2}} e^{-\frac{2w_0^2(z)\cos^2\theta\tau^2}{w^2(z)}} \right], \quad (21)$$

number fluctuation term

where $\langle N \rangle$ is the average number of particles in the scattering volume. In OCT, $\langle N \rangle$ corresponds to the depth-resolved number of particles per scattering volume and is a function of axial position z through the shape of the probing beam. Equation (21) is based on the same assumptions as Eq. (8), except that there is no restriction on the number of particles. Number fluctuations only affect $g_2(z, \tau)$ and have no influence on $g_1(z, \tau)$ [7,8]. The number fluctuation term in Eq. (21) does not depend on diffusion, i.e., flow and diffusion decorrelations are decoupled. In general, there are diffusional number fluctuations in $g_2(z, \tau)$ [21,22], however, the relevant time delays for these fluctuations are much larger than flow decorrelation times as they depend on the ratio of lateral resolution over diffusional displacement. With typical spatial resolutions and diffusion coefficients, these diffusive fluctuations can be neglected in the presence of flow. In contrast to the non-dilute case, the number fluctuation decay rate depends on the local beam waist, $w(z)$, and not the beam waist in focus, w_0 . The expected number of particles in the scattering volume, $\langle N \rangle$, is a function of the PSF and the particle volume fraction f_v , and is given by

$$\langle N \rangle = \frac{3f_v V_s}{4\pi a^3}, \quad (22)$$

where a is the particle radius and V_s is the scattering volume which appears as the normalization factor in $g_2(\tau, z)$. The depth-dependent V_s , found by integrating the intensity PSF over all space, is [8]

$$V_s = 2\pi \int_0^\infty e^{-\frac{4r^2}{w^2(z)}} r dr \int_{-\infty}^\infty e^{-\frac{2z^2}{w_z^2}} dz \approx \frac{\pi^{3/2} w^2(z) w_z}{2^{5/2}}, \quad (23)$$

where the factor 2π in front of the integral originates from rotational symmetry of the lateral PSF. Since the coherence function waist w_z is much smaller than length scales at which the local beam

waist varies significantly, $w(z)$ was assumed to be constant within the integral over the axial PSF. Combining Eq. (22,23) we find

$$\langle N \rangle = \frac{3f_v \sqrt{\pi} w^2(z) w_z}{2^{9/2} a^3}. \quad (24)$$

Since the OCT signal is discrete in depth, $w(z)$ is also assumed to be constant within every voxel.

For sufficiently small $\langle N \rangle$ and flow decorrelation much smaller than diffusion decorrelation ($\tau_{v_0} \gg \tau_D$), as given by Eq. (9,10), the normalized second-order autocovariance function at larger time delays, when the Gaussian term has already decayed, is completely dominated by the number fluctuations term given by

$$g_2(z, \tau \gg \tau_D) \approx \frac{1}{\left(1 + \frac{1}{\text{SNR}(z)}\right)^2} \frac{1}{2^{3/2} \langle N \rangle + 1} e^{-\frac{v_0^2(z) \sin^2 \theta \tau^2}{w_z^2}} e^{-\frac{2v_0^2(z) \cos^2 \theta \tau^2}{w^2(z)}}, \quad (25)$$

Therefore, for slowly flowing dilute samples, $g_2(z, \tau)$ decorrelation at larger time delays is independent of the particle diffusion and depends only on the particle flow speed. In this regime, the minimum measurable velocity is limited only by SNR. The minimum measurable velocity can be obtained by neglecting the diffusion and using only the SNR part from Eq. (19) in Sec. 2.2.

2.4. Flow speed sensitivity analysis

Theoretical velocity sensitivities of Doppler OCT, non-dilute DLS-OCT, and number fluctuation DLS-OCT for Doppler angles of up to 10° are plotted in Fig. 2. The sensitivity is quantified as δv_0 indicating the minimum measurable flow velocity and plotted versus SNR. The calculated sensitivities are based on the diffusion coefficient of $9.08 \times 10^{-13} \text{ m}^2/\text{s}$, which is equivalent to a particle radius of 242 nm (average of the measurements in Table 1). In the calculations the following experimental values, as given in Sec. 3, were used: $M = 6 \times 30999$, $w(z)$, w_0 , and Δt .

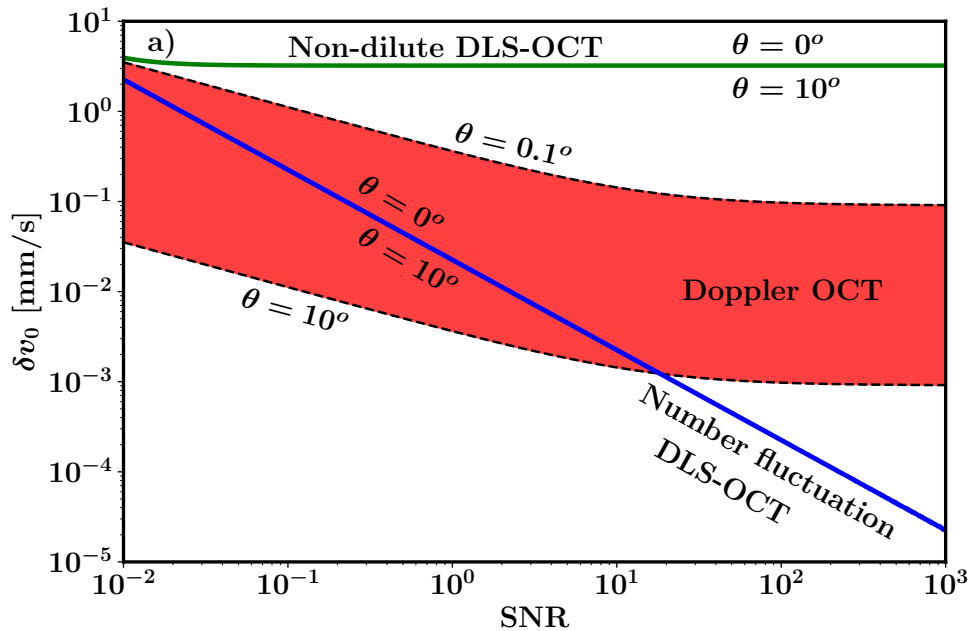


Fig. 2. Velocity sensitivities as a function of SNR and θ for Doppler OCT, non-dilute DLS-OCT, and number fluctuation DLS-OCT.

Non-dilute and number fluctuation DLS-OCT methods show minimal dependence on θ as these methods work for any angle. In contrast, the Doppler OCT sensitivity strongly depends on the Doppler angle with large angles resulting in a large phase shift and therefore a higher sensitivity (lower δv_0).

According to Eq. (4–6), the sensitivity of Doppler OCT is limited by SNR and particle diffusion, with both factors being independent of each other. In Fig. 2 we see that the Doppler OCT sensitivity levels off at higher SNR values ($\text{SNR} > 10$) as the diffusive limit is reached. At this stage it is no longer possible to improve the velocity sensitivity by increasing the SNR. Equations (12,17–19) show that non-dilute DLS-OCT is also limited by the same factors, but its diffusion limitation is much more restrictive. This is clearly visible in Fig. 2 where the sensitivity of this method is almost independent of SNR.

For the number fluctuation DLS-OCT the minimum measurable velocity follows the same derivation as for DLS-OCT, only there is no dependence on diffusion in Eq. (19). Figure 2 shows that its velocity sensitivity is only a function of SNR and does not level off to a constant value as it does in a diffusion-limited scenario like Doppler OCT or non-dilute DLS-OCT. For SNRs higher than 10, number fluctuation DLS-OCT has a higher sensitivity than Doppler OCT even at relatively large θ . The amount of improvement is related to the Doppler angle due to dependence of Doppler OCT sensitivity on θ .

2.5. Number fluctuation particle concentration estimation

Number fluctuations in DLS-OCT also can be used to determine particle concentration in a sample through the dependence of $g_2(z, \tau)$ on $\langle N \rangle$. For time delays with negligible number fluctuation flow decorrelation, the normalized second-order autocovariance function can be approximated as

$$g_2(z, \tau \ll \tau_{v_0}) \approx \frac{2^{3/2} \langle N \rangle}{2^{3/2} \langle N \rangle + 1} |g_1(z, \tau \ll \tau_{v_0})|^2 + \frac{1}{\left(1 + \frac{1}{\text{SNR}(z)}\right)^2} \frac{1}{2^{3/2} \langle N \rangle + 1}, \quad (26)$$

where the limiting time delay τ_{v_0} is given by Eq. (10). From Eq. (26) we can obtain the particle concentration by solving for $\langle N \rangle$

$$\langle N \rangle \approx \frac{\frac{1}{\left(1 + \frac{1}{\text{SNR}(z)}\right)^2} - g_2(z, \tau \ll \tau_{v_0})}{2^{3/2} \left[g_2(z, \tau \ll \tau_{v_0}) - |g_1(z, \tau \ll \tau_{v_0})|^2 \right]}, \quad \text{with} \quad (27)$$

$$\frac{1}{\left(1 + \frac{1}{\text{SNR}(z)}\right)^2} = |g_1(z, \tau = 0)|^2. \quad (28)$$

Here $g_1(z, \tau = 0)$ is an extrapolation of the fit to the first-order normalized autocovariance function at $\tau = 0$. Note that $\langle N \rangle$ can be determined for any $\tau \ll \tau_{v_0}$, but that for practical applications it is averaged over all relevant times. Alternatively, $\langle N \rangle$ can also be calculated using

$$\langle N \rangle = \frac{|g_1(z, \tau = 0)|^2}{2^{3/2} g_2(z, \tau = 0)_{\langle N \rangle}} - 2^{-3/2}, \quad (29)$$

where $g_2(z, \tau = 0)_{\langle N \rangle}$ is the extrapolation of the fit to the number fluctuation term ($\tau \gg \tau_D$) of the second-order normalized autocovariance function at $\tau = 0$.

3. Materials and methods

3.1. OCT system

The experiments were performed using a Thorlabs GANYMEDE II HR series spectral domain OCT System, which has been described in detail in our previous work [23]. The acquisition rate was 5.5 kHz. The same datasets and time series were used both in number fluctuation DLS-OCT and Doppler OCT analyses. The OCT axial resolution and axial decorrelation were determined using the wavenumber spectrum standard deviation, σ_k , of the measured reference spectrum. The acquired signal spectrum was measured with a spectrometer with 2048 pixels. After acquisition, the measured spectrum was first resampled to a linearly-sampled wavenumber domain and then apodized using a Gaussian filter. After the apodization, the measured coherence function waist in sample was $w_z = 2.11 \mu\text{m}$. We have neglected the effect of a gradient of the axial velocity on the autocovariance function for two reasons [24]. First, the Doppler angles in this work are low ($\theta < 2^\circ$). Second, our optical resolution is high both in axial and transverse directions. Hence, the flow velocity within PSF can be assumed to be constant.

The OCT system is operated with a scan lens (LSM04-BB, Thorlabs) in a confocal setup with a manufacturer provided focal spot size of $w_0 = 6 \mu\text{m}$ in air which was validated by axial confocal response measurements, defined as the e^{-2} radius of the intensity function. The measured values were around $w_0 = 5 - 6 \mu\text{m}$. The NA of the system was 0.05. Depending on the angle of incidence, refractive index contrast and Gaussian beam parameters, w_0 and $w(z)$ vary somewhat because of the passage of the beam through the interfaces [25]. Therefore, for each experiment, $w(z)$ was calibrated using the procedure described in Sec. 3.4. For minimizing the number of particles within the scattering volume, $\langle N \rangle$, the beam waist was placed at the center of the flow channel in depth [8]. Since for the given OCT setup the coherence length and the NA are very low, it can be assumed that the scattering angle is 180° and the scattering wavenumber q in the correlation analysis is constant at $q = 2nk_0$.

Determination of the particle number density $\langle N \rangle$ using Eq. (27–29) requires a-priori knowledge or an estimate of the system SNR. In this work we estimated the SNR at every depth using a fit to the measured $g_1(z, \tau)$, as described in Sec. 3.4. If required, the depth-resolved SNR can be measured a-priori according to the procedure described in [6]. We used this approach to verify the obtained SNR values in the particle suspension that were around 3 – 30.

3.2. Flow system

The flow was generated using a syringe pump with variable discharge rate (Fusion 100, Chemyx, Inc.) and a 1 mL syringe (BD Plastipak). The flow passes through a quartz rectangular flow cell with internal dimensions of 0.5 mm thickness and 10 mm width (type 45-F, Starna Scientific). Every experiment was performed using a 0.005% volume fraction of dilute suspension of monodisperse polystyrene particles in water. The particles were supplied by InProcess-LSP with an expected radius of 257 nm. Since the particle solution was extremely dilute, the refractive index and viscosity of the sample as a function of wavelength were assumed to be identical to water at room temperature and calculated using equations from [26,27]. The sample temperature was assumed to be 21°C , corresponding to a water refractive index of $n = 1.33$. As a reference, velocity profiles for the set pump discharge rates were calculated using the analytical solution for the Poiseuille flow in a rectangular channel [28]

$$v(y, z) = \frac{Q}{75\pi^3 h w (1 - 0.63 \frac{h}{w})} \sum_{m=1, m \text{ odd}}^{\infty} \frac{\sin(\frac{m\pi z}{h})}{m^3} \left[1 - \frac{\cosh(m\pi \frac{y}{h})}{\cosh(m\pi \frac{w}{2h})} \right], \quad (30)$$

$$v(y = 0, z) \approx \frac{Q}{75\pi^3 h w (1 - 0.63 \frac{h}{w})} \sum_{m=1, m \text{ odd}}^{\infty} \frac{\sin(\frac{m\pi z}{h})}{m^3}, \quad (31)$$

where the velocity, in mm/s, is given as a function of depth z and lateral position y , w is the width of the flow cell in mm, h is the flow cell thickness in mm ($h < w$) and Q is the pump discharge rate in $\mu\text{L/s}$. In the analytical solution, the maximum velocities are observed at the half-width of the cell at $y = 0$. Therefore, in 1D measurements, the OCT beam focal plane was positioned as close as possible to this location to ensure a maximum decorrelation. We performed 1D flow measurements for discharges in the range of 0 – 3.33 $\mu\text{L/s}$ at three different Doppler angles. The corresponding expected flow velocities in the channel were in between 0 – 1 mm/s. For 2D measurements only one Doppler angle was considered.

3.3. Doppler OCT flow measurements

Doppler OCT analysis was performed as follows: First, OCT spectra were acquired with a time series length of 31000, resulting in an acquisition time of 5 – 6 seconds and a sampling time of $\Delta t = 5500^{-1}$ s. This measurement was repeated 6 times, resulting in $M = 6 \times 30999$ phase/intensity changes. For each time series a DC component was calculated by averaging all spectra. Second, the interference spectra were computed by subtracting the DC component from the acquired spectra. Third, a complex depth-resolved OCT signal was obtained using the inverse Fourier transformation of the interference spectra. Finally, axial velocities were determined with Eq. (2) using a phase estimation through

$$\Delta\phi(z) = \left\langle \tan^{-1} \left[\frac{\text{Im}(a(z, t) \times a^*(z, t + \Delta t))}{\text{Re}(a(z, t) \times a^*(z, t + \Delta t))} \right] \right\rangle_t, \quad (32)$$

where $a(z, t)$ and $a(z, t + \Delta t)$ represent the complex OCT data at times t and $t + \Delta t$, respectively. The $\langle \cdot \rangle_t$ denotes the time averaging. All phase measurements were used in the analysis. Total flow velocities were determined by dividing the axial velocities with $\sin \theta$. The Doppler angle calibration procedure is described in Sec. 3.4.

3.4. Number fluctuation DLS-OCT flow measurements

In number fluctuation DLS-OCT the first three processing steps were the same as in the Doppler OCT analysis from Sec. 3.3. However, instead of determining the OCT phase, the magnitude of a complex OCT signal was calculated. Normalized temporal fluctuations of the scattered signal magnitude from dilute and non-dilute samples are shown in Fig. 3(a). The non-dilute OCT signal shows relatively small deviations from the mean. In contrast, the number-fluctuation OCT signal shows much larger signal variations, with a clear spike-like behavior due to particles moving in and out of the focal area. With the non-dilute sample, complex field fluctuations due to the Brownian motion of the particles follows Gaussian statistics. Hence, the field magnitude fluctuations have a Rayleigh distribution as shown in Fig. 3(b). In the dilute regime the OCT signal magnitude is directly proportional to the number of particles where the number of particles in the scattering volume follows the Poisson distribution [7,8]. Therefore, it is expected that the magnitude fluctuations due to number fluctuations are also Poisson distributed, as shown in Fig. 3(b).

After determining field magnitude fluctuations for each acquisition, a normalized second-order autocovariance of the mean-subtracted signal magnitude was calculated at every depth. The autocovariance functions were averaged for all 6 acquisitions. Finally, Eq. (33) was fitted to the averaged autocovariance functions with

$$g_2(z, \tau > \tau_N) = A(z) e^{-\frac{v_0^2(z) \sin^2 \theta \tau^2}{w^2}} e^{-\frac{2v_0^2(z) \cos^2 \theta \tau^2}{w^2(z)}}, \quad (33)$$

where the choice of free parameters depended on whether calibration or flow measurements were performed. In our fitting procedure only the number fluctuation term was fitted. To ensure that

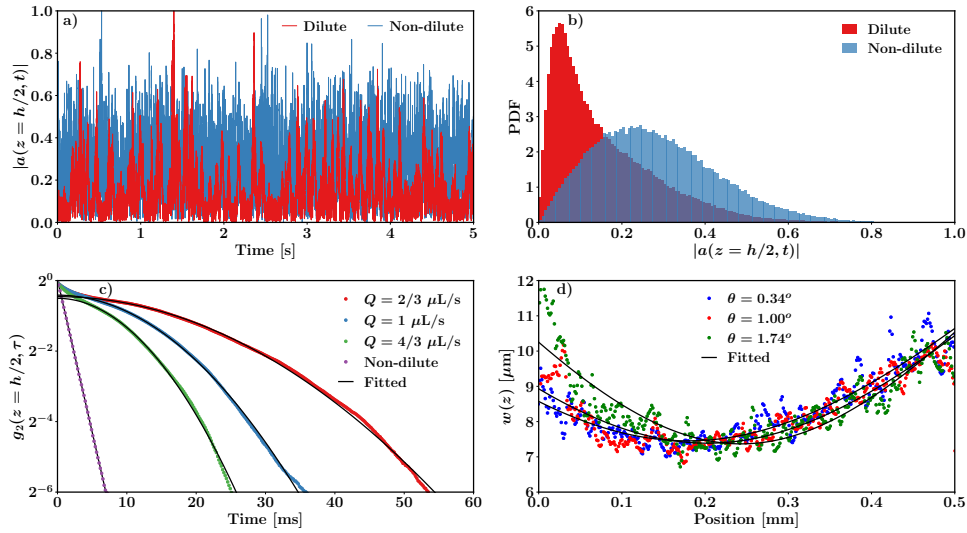


Fig. 3. (a-b) Time trace and distribution of the OCT signal magnitude from non-dilute (0.5%) and dilute (0.005%) samples at $Q = 1 \mu\text{L/s}$ and $\theta = 0.34^\circ$. (c) Measured and fitted $g_2(z, \tau)$ for non-dilute and dilute samples at different flow rates and $\theta = 0.34^\circ$. (d) Measured and fitted beam waist at different Doppler angles.

the diffusive term in the measured autocovariance had decayed sufficiently, only $g_2(z, \tau > \tau_N)$ was considered, where τ_N was the time delay with $g_2(z, \tau > \tau_N) > 10 \cdot |g_1(z, \tau > \tau_N)|^2$. Examples of the measured and fitted second-order autocovariance functions from the dilute sample at different discharge rates are shown in Fig. 3(c). For comparison, a diffusion-dominated $g_2(z, \tau)$ from the same, but more concentrated, sample is also shown. In non-dilute DLS-OCT $g_2(z, \tau)$ decays exponentially (linearly on a logarithmic scale) at low flow speeds. In number fluctuation DLS-OCT the decay is much slower and quadratic on a logarithmic scale, where the effect of a particle diffusion is visible for the Gaussian term at very small time delays with $\tau < \tau_N$. As Fig. 3(c) shows, the fit models match very well with the number fluctuation term of the normalized autocovariance functions at different flow rates.

To perform quantitative number fluctuation measurements, the beam waist $w(z)$ and the Doppler angle θ were determined in a two-step procedure. During the first step, a beam waist calibration was performed, as described in [23]. The beam was moved with a-priori known velocity over a stationary sample while the spectra were acquired. The local beam waist $w(z)$ was determined using a fit of Eq. (33) to the measured $g_2(z, \tau > \tau_N)$ with $A(z)$ and $w(z)$ being the free parameters. The obtained beam profiles for different Doppler angles are shown in Fig. 3(d). Here the beam shapes were fitted using $w(z) = w_0 \sqrt{1 + ((z - z_0)/z_R)^2}$, with w_0 , z_0 , and z_R being the free parameters. The fitted beam waist values are given in Table 1.

In the second step, the Doppler angle was determined. For this purpose any flow measurement with a sufficient Doppler signal could be used. Here $v_z(z)$ was determined using the phase-resolved Doppler analysis from Sec. 3.3. Then Eq. (33) was fitted to the measured $g_2(z, \tau > \tau_N)$, incorporating the known $w(z)$ and $v_z(z)$ while using $A(z)$ and $v_r(z)$ as free parameters. The depth-averaged angle was then determined using $\theta = \langle \arctan(v_z(z)/v_r(z)) \rangle_z$. The obtained Doppler angles are given in Table 1. After these two calibration steps, flow measurements could be performed for the given geometry at any discharge rate. For each flow rate Eq. (33) was fitted to the measured $g_2(z, \tau > \tau_N)$ using $A(z)$ and $v_0(z)$ as the only fit parameters.

Table 1. Measured Doppler angle, particle radius, and beam waist for the four experimental conditions.

Mode	θ [°]	a [nm]	w_0 [μm]
1D	0.34 ± 0.01	233 ± 8	7.45 ± 0.03
1D	1.00 ± 0.05	247 ± 11	7.39 ± 0.03
1D	1.74 ± 0.02	246 ± 11	7.37 ± 0.05
2D	1.84 ± 0.08	NA	7.79 ± 0.07

The number of particles in the scattering volume was obtained without any a-priori calibration or SNR measurements. Particle number density under flow was determined at the discharge rates of 1/12 and 1/6 μL/s using Eq. (29), incorporating the fitted and extrapolated values $g_2(z, \tau = 0)_{\langle N \rangle}$ and $g_1(z, \tau = 0)$. The number fluctuation term of $g_2(z, \tau)$ was fitted using Eq. (33), and $g_1(z, \tau)$ was fitted using Eq. (34)

$$|g_1(z, \tau)| = \frac{1}{1 + \frac{1}{\text{SNR}(z)}} e^{-Dq^2\tau}, \quad (34)$$

with $\text{SNR}(z)$ and D being the free parameters. Here we have neglected the contribution from the flow decorrelation, because $g_1(z, \tau)$ is diffusion-dominated at these flow rates and independent of number fluctuations. As a reference, the particle diffusion coefficient D was determined from the fit of Eq. (34) to the measured $g_1(z, \tau)$ from the stationary fluid at all Doppler angles. The diffusion coefficient is irrelevant for flow or number density measurements with the number fluctuation term of $g_2(z, \tau)$. However, it is required for determining the particle size which is used for calculating the theoretical $\langle N \rangle$ from a known particles' volume fraction. Particle radii determined using the Stokes-Einstein relation are given in Table 1 and match the particle radius of 257 nm from the provider reasonable well.

2D flow measurements with number fluctuation DLS-OCT were performed by lateral scanning of the OCT beam along the flow cell, perpendicular to the flow direction. Even though the channel width was 10 mm, only 2 mm was imaged due to sampling limitations and the presence of aberrations. For resolving the transverse flow profile the scanning location was chosen near the flow cell edge. For 2D measurements 2000 consecutive B-scans were acquired with 100 lateral points in each scan, resulting in the total acquisition time of 44 s. Data processing steps were the same as before. However, instead of correlating the field magnitude fluctuations at a single position, the temporal autocovariance at each location in the B-scan was performed. This reduced the effective sampling rate from 5.5 kHz to approximately 45 Hz at each location in the 2D measurement. This sampling rate was still sufficiently fast to determine the flow from the number fluctuation autocovariance and enabled the implementation of number fluctuation flow imaging in conventional B-scan mode.

4. Experimental results

Three sets of 1D measurements were performed at the center of the flow cell for θ values of 0.34° , 1.00° and 1.74° . For each angle, the pump discharge rate was varied from 1/12 to 10/3 μL/s. Figure 4 shows velocity profiles obtained with number fluctuation DLS-OCT (top row) and phase-resolved Doppler OCT (bottom row). The parabolic curves represent the expected velocity profiles according to Eq. (31), the flow channel dimensions and the discharge rate. To quantitatively compare both methods, all measured velocities at a fixed angle are plotted against the expected velocities in Fig. 5, where the black curves corresponds to the expected values.

Figures 4(a,d) and 5(a) show the number fluctuation DLS-OCT and Doppler OCT flow measurements for $\theta = 0.34^\circ$. The Doppler OCT sensitivity is very low, making it impossible to

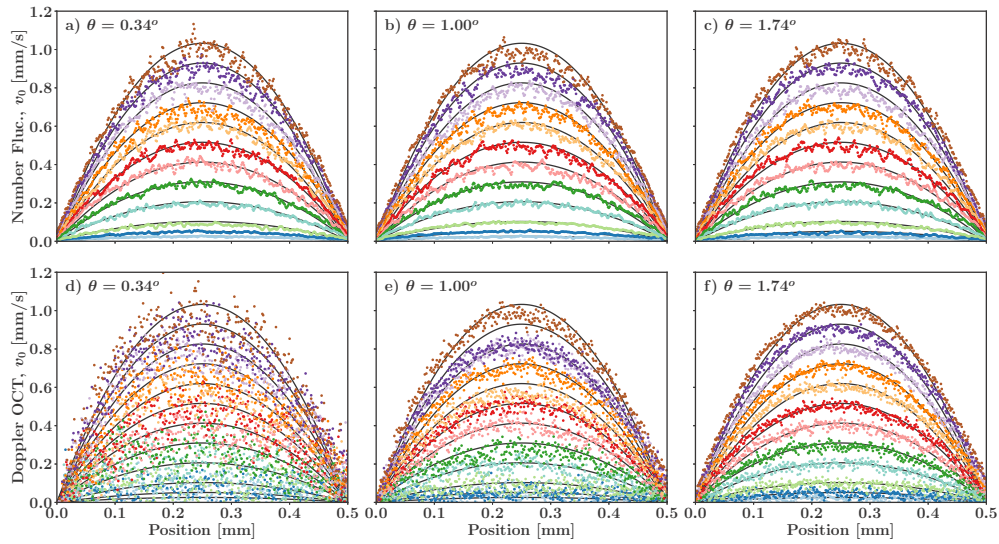


Fig. 4. Flow profiles measured using different methods. (a-c) Number fluctuation DLS-OCT. (d-f) Phase-resolved Doppler OCT.

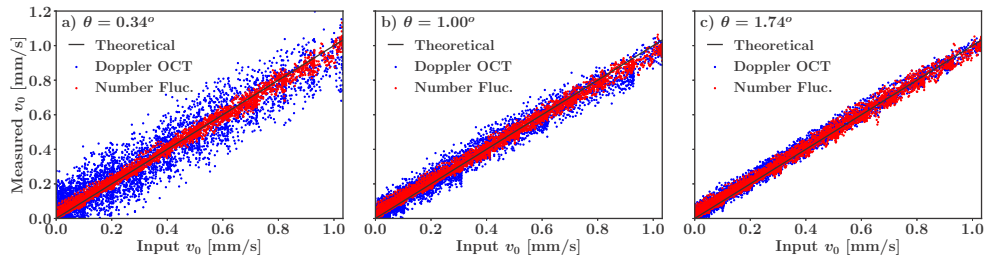


Fig. 5. Measured versus input velocities for (a) $\theta = 0.34^\circ$, (b) $\theta = 1.00^\circ$, and (c) $\theta = 1.74^\circ$.

accurately measure flow velocities for these low axial speeds. This is clearly indicated by the spread of measurements in Fig. 5(a). The number fluctuation DLS-OCT method, on the other hand, can accurately determine flow velocities for all considered flow speeds.

Figures 4(b,e) and 5(b) show the same measurements for $\theta = 1.00^\circ$. In this case, the Doppler OCT sensitivity is higher but still insufficient to fully resolve the flow for the different discharge rates. The spread of measurements in Fig. 5(b) is therefore also lower compared to Fig. 5(a). The accuracy of the number fluctuation DLS-OCT method is unchanged. This is indicated by accurate reconstruction of flow profiles in Fig. 4(b) and low spread of measurements in Fig. 5(b).

Figures 4(c,f) and 5(c) show the flow measurements for $\theta = 1.74^\circ$. In this case the sensitivity of Doppler OCT is much better due to the larger axial flow component. Performance is comparable to number fluctuation DLS-OCT for higher discharge rates, but very low velocities are still poorly resolved. For low flow velocities, number fluctuation DLS-OCT technique has a superior performance compared to Doppler OCT and also can work for zero Doppler angle.

The sensitivity of Doppler OCT strongly depends on the Doppler angle, and the minimum measurable velocity decreases with increasing θ . For number fluctuation DLS-OCT, the sensitivity is independent of the Doppler angle, which is in agreement with our expectations from Sec. 2.1 and 2.3. Number fluctuation DLS-OCT can accurately determine flow velocities for all considered flow speeds whereas the flow profiles cannot be accurately measured using non-dilute DLS-OCT,

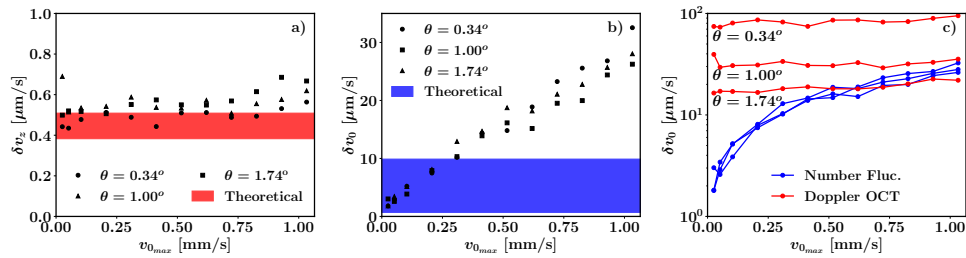


Fig. 6. (a) Measured and expected axial velocity sensitivities for Doppler OCT, (b) measured and expected total velocity sensitivities for number fluctuation DLS-OCT, and (c) measured total velocity sensitivities for both methods versus the maximum profile velocity.

as the profile velocities are well below the limit set by diffusion, which is approximately 3.3 mm/s for our experimental setup and used Doppler angles.

In Fig. 6 we compare the measured accuracy with the expected velocity sensitivities according to the theory outlined in Sec. 2.1–2.3. The maximum velocity (at the center of the profile) was calculated for each discharge rate according to Eq. (31) and plotted on the x -axis. For each discharge, the velocity uncertainty was estimated by calculating the velocity profile standard deviation with respect to the best fit parabolic curve. For direct comparisons with the theoretical minimum measurable velocities, an SNR range of 3 – 30 was used as determined from the measurement data. Figure 6(a) shows that for Doppler OCT, the obtained absolute axial velocity sensitivity is independent of Doppler angle and maximum profile velocity (discharge rate), and the minimum measurable axial velocities are slightly higher than expected. Invariance of the axial velocity sensitivity with respect to the discharge rate is expected, since it is independent of the Doppler phase shift magnitude. In Fig. 6(b) we see that the velocity sensitivity for number fluctuation DLS-OCT is independent of θ but changes with increasing maximum profile velocity. At low flow rates, corresponding to long decorrelation times, the measured sensitivities have the same order of magnitude as the theoretical ones for intensity fluctuations. However, the deviation increases at higher velocities when the number of relevant fit points becomes lower and fit errors increase. Figure 6(c) shows the estimation of the total velocity. Clearly, number fluctuation DLS-OCT is more accurate for low flow rates as would be expected from the calculated flow sensitivity advantage for constant SNR as shown in Fig. 2. In addition, the flow estimate does not depend on Doppler angle. This makes it easier to quantify the total flow, which is the relevant parameter.

The number of particles in the scattering volume, $\langle N \rangle$, was obtained using Eq. (29) for the lowest two discharge rates, 1/12 and 1/6 $\mu\text{L/s}$, respectively. The expected number of particles was calculated using Eq. (24) incorporating the particle radius from Table 1 and other optical/sample

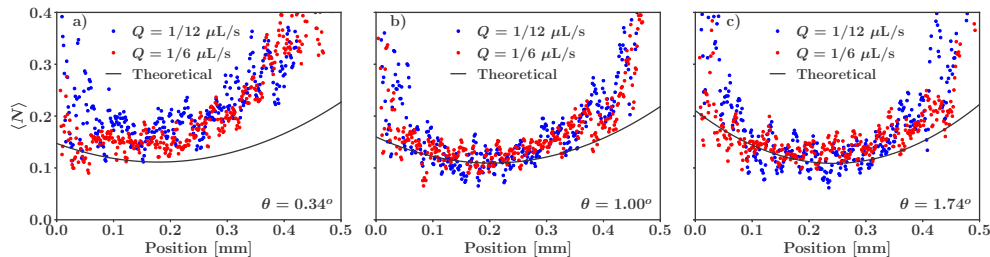


Fig. 7. Depth-resolved number of particles in the scattering volume for (a) $\theta = 0.34^\circ$, (b) $\theta = 1.00^\circ$, and (c) $\theta = 1.74^\circ$.

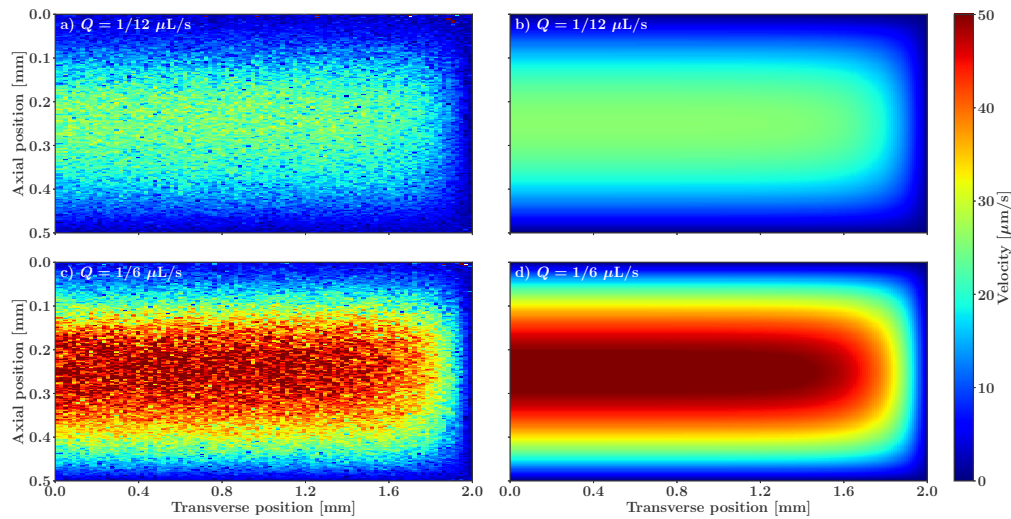


Fig. 8. Measured (a) and expected (b) 2D velocity profiles for $Q = 1/12 \mu\text{L/s}$. Measured (c) and expected (d) flow profiles for $Q = 1/6 \mu\text{L/s}$.

properties. Figure 7 shows that the obtained number of particles in the focal area, $\langle N \rangle$, matches well with the expected distribution at positions close to beam waist. Deviations increase towards the flow cell edges where the SNR is lower and the local beam waist is larger. There is no explicit dependence on the Doppler angle and the average number of particles within the scattering volume is much lower than 1. As expected, $\langle N \rangle$ is minimum near the beam waist and is higher away from focus. Almost identical results are obtained when measuring SNR a-priori or when Eq. (27,28) are used. The measured number of particles per scattering volume can easily be converted to volume fraction using the particle size and scattering volume. Values of $\langle N \rangle$ from the central portions of Fig. 7 with a higher SNR correspond to particle volume fractions 0.004 – 0.007%. This is in good agreement with the expected volume fraction of 0.005%.

2D flow measurements were performed at the flow cell edge for $\theta = 1.84^\circ$ and the pump discharge rates of 1/12 and 1/6 $\mu\text{L/s}$. Figure 8 shows transverse and axial velocity profiles obtained using number fluctuation DLS-OCT (left column) and expected flow profiles according to Eq. (30) (right column). The obtained velocity distributions are in good agreement with the expected values and both the transverse and the axial flow profiles are clearly visible. The transverse flow profile is uniform except very close to the flow cell edge at distances less than 0.4 mm, whereas the axial velocity profile has a much larger degree of variation. Due to the limitations imposed by particle diffusion, flow profiles for such low flow velocities can be obtained neither by Doppler OCT nor by non-dilute DLS-OCT.

5. Discussion

Our results show that number fluctuation DLS-OCT can significantly improve the velocity sensitivity compared to current Doppler OCT flow measurements. While phase-resolved Doppler OCT and non-dilute DLS-OCT are ultimately limited by particle diffusion, our method allows sub-diffusion flow velocity measurements with a sensitivity only limited by the SNR. Moreover, our method works for arbitrary Doppler angle and has a clear advantage in situations where the number density of scattering particles in the sample is very low while sufficient light is scattered. The advantage of number fluctuation DLS-OCT decreases with increasing Doppler angles. As

Fig. 2 shows, Doppler OCT can be more sensitive at high θ values. The exact crossover point depends on system parameters and resolution. However, sufficiently increasing the Doppler angle is difficult due to several reasons: First, with larger θ , beam refraction effects and a sensitivity loss in depth become more pronounced. Second, higher flow speeds can cause phase wrapping and distortion [10], leading to incorrect phase estimation. Third, in certain applications θ may be limited to small angles due to geometric constraints, for example in medical and ophthalmic imaging. Therefore, it is preferable to use low Doppler angles at which our method has a superior performance than Doppler OCT. The low angle also allows to neglect gradient effects on the normalized autocovariance function [24].

In very dilute samples the number of scattering particles is very low. However, due to bulk flow, scatterers always move from one OCT voxel to another, which has a temporal averaging effect over the whole acquisition period. So, even though the average number of scatterers per voxel is around 0.1 – 0.2, there is still a sufficient scattered signal from each voxel for capturing number fluctuations. In fact, with our OCT system we could measure even more dilute samples. Yet, going to lower concentrations reduces SNR and makes OCT flow measurements more difficult. To estimate phase changes accurately with Doppler OCT at low flow speeds and low θ , we averaged over long acquisition times. Relatively large time traces are also needed to reduce the statistical bias [19] of $g_2(z, \tau)$ in number fluctuation DLS-OCT when dealing with slow flows. In this work, the measurement time series length was chosen based on an accurate flow estimation for the lowest considered discharge rate. However, the time series length could in principle be reduced for faster flows allowing for faster 1D and 2D imaging. We have also noticed that acquiring several time traces for averaging was more critical for Doppler OCT than for number fluctuation DLS-OCT.

The flow profiles obtained for Doppler and number fluctuation DLS-OCT methods match well with the expected flow velocities. Uncertainties in the flow can be attributed to the beam waist calibration, beam offset from the center of the flow channel and the pump stability [23], which have an effect especially at very low discharge rates. As Fig. 6 shows, the sensitivity of Doppler OCT for varying velocity is constant, implying that systematic errors are minimal and do not increase with increasing flow rates. Small deviations from the expected sensitivity range could be caused by a fact that the system is not shot-noise limited or the phase stability is less than ideal. In contrast to our derived model, the velocity uncertainties in number fluctuation DLS-OCT increase as a function of flow (discharge) rate, indicating that the method accuracy drops for larger velocities. The theoretical framework for SNR-based sensitivity analysis of number fluctuation DLS-OCT given in Sec. 2.3 is based on the minimum measurable relative intensity change when particles move during a single time step and assuming a factor \sqrt{M} over M measurements. It does not take into account additional factors introduced when computing the normalized autocovariance of intensity fluctuations, such as the statistical or the fit model bias due to a limited number of time series points. As the flow speed increases, the autocovariance decay becomes more rapid and there are fewer sampling points available for fitting. In addition, with increasing flow velocity the difference in decay rates between the Gaussian and number fluctuation terms in $g_2(z, \tau)$ decreases, making extraction of the number fluctuation term more difficult. Our theoretical model gives an estimation of the order of magnitude of the minimum measurable velocity. It can be further extended by including the above-mentioned factors for more accurate flow measurement sensitivity analysis. For best performance, number fluctuation DLS-OCT should be implemented in the diffusion-dominated regime for very low flow rates with

$$v_0 \sqrt{\frac{\sin^2 \theta}{w_z^2} + \frac{2 \cos^2 \theta}{w_0^2}} \ll 2Dq^2. \quad (35)$$

In contrast, for faster flows where

$$v_0 \sqrt{\frac{\sin^2 \theta}{w_z^2} + \frac{2 \cos^2 \theta}{w_0^2}} \gg 2Dq^2, \quad (36)$$

non-dilute DLS-OCT or even scanning DLS-OCT [23] are more suitable methods. With intermediate flow regimes where

$$v_0 \sqrt{\frac{\sin^2 \theta}{w_z^2} + \frac{2 \cos^2 \theta}{w_0^2}} \sim 2Dq^2, \quad (37)$$

both techniques can be combined for improved accuracy.

Number fluctuation DLS-OCT can be utilized for simultaneous 2D velocimetry of sub-diffusion flows using scanning OCT systems. This is impossible for Doppler OCT or non-dilute DLS-OCT due to particle diffusion and sampling limitations. Even though the sampling frequency of adjacent B-scans is significantly reduced compared to single point measurements, it is still sufficient for resolving sub-diffusion flows since the number fluctuation decorrelation is very slow. This shows the feasibility of this technique for volumetric flow imaging even with limited acquisition rates. In contrast, it is impossible to measure 2D flow profiles with so low sampling speed at any flow velocity using Doppler OCT or non-dilute DLS-OCT. In this case, the low-speed flows are dominated by diffusion, and much higher sampling rates are required for measuring faster flows.

Reliability of number fluctuation DLS-OCT increases with increasing relative weight of the number fluctuation term in Eq. (21). The relative weight of this term can be increased by decreasing the particle density in the sample and/or increasing the particle radius. For a fixed particle volume fraction, increasing particle size leads to fewer particles in the scattering volume, $\langle N \rangle$, but increases scattered light power (higher SNR) per particle due to the scaling of the Mie/Rayleigh scattered intensity ($I_s \sim a^6$). The latter effect is more dominant, resulting in higher total scattered power and a larger contribution of the number fluctuation term to the normalized autocovariance function. However, a larger particle size leads to slower diffusive decorrelation. As a result the Gaussian and number fluctuation terms can have similar decorrelation ranges for the same flow speed.

Applications of number fluctuation DLS-OCT are not limited to extremely dilute samples. Our method can also be used to measure low-speed flows of typical pharmaceutical, biological or rheological suspensions that are imaged with OCT. Here we foresee two possible implementations: First, a non-dilute sample can be seeded with a small number of relatively large and highly scattering particles, ensuring low $\langle N \rangle$ but sufficient measurement SNR. In this way the number fluctuation term can be measured without changing the OCT system. The second option is to improve the number fluctuation term contrast optically by increasing the numerical aperture (NA) and reducing the scattering volume. In this case the original, unseeded sample can be used but a higher resolution OCT system is required. Note that an increase in optical resolution comes at the expense of a decrease in the effective axial working range.

Number fluctuation DLS-OCT can be used to determine the average number of scatterers in the scattering volume, $\langle N \rangle$, which is directly related to the particle concentration. This can be performed without any a-priori measurements. In this case a high axial resolution is preferable for maximizing $\langle N \rangle^{-1}$ and therefore the importance of the number fluctuation term. We expect that for a digitized OCT signal, Eq. (24) is only valid if the coherence waist and the axial pixel pitch are small compared to the length scales at which the local beam waist varies significantly. When using Eq. (27) for estimating $\langle N \rangle$, the flow decay in the measured $g_1(z, \tau)$ and $g_2(z, \tau)$ must be negligible ($\tau \ll \tau_{v_0}$). Equation (29), on the other hand, is independent of the flow decay time and therefore easier to implement for determining $\langle N \rangle$, but requires additional extrapolation of the data.

6. Conclusion

We have implemented number fluctuation DLS-OCT for measuring sub-diffusion, low-speed flows in dilute particle suspensions using the second-order autocovariance function. Our method extends the minimum measurable velocity limit compared to the standard non-dilute DLS-OCT or Doppler OCT techniques and completely removes the limitation on the minimum measurable flow due to diffusive motion of the particles. We have shown that our method is independent of the Doppler angle, is applicable to 2D flow velocimetry in a scanning OCT setup, and can be used to determine particle concentration in flowing dilute suspensions.

Funding. NWO Domain Applied and Engineering Sciences (17988).

Acknowledgments. We would like to thank InProcess-LSP for their support and discussions.

Disclosures. The authors declare no conflicts of interest.

Data availability. Data underlying the results presented in this paper and the relevant analysis routines are available at [29].

References

1. J. Kalkman, R. Sprik, and T. G. van Leeuwen, "Path-length-resolved diffusive particle dynamics in spectral-domain optical coherence tomography," *Phys. Rev. Lett.* **105**(19), 198302 (2010).
2. N. Weiss, T. G. van Leeuwen, and J. Kalkman, "Localized measurement of longitudinal and transverse flow velocities in colloidal suspensions using optical coherence tomography," *Phys. Rev. E* **88**(4), 042312 (2013).
3. J. Lee, W. Wu, J. Y. Jiang, B. Zhu, and D. A. Boas, "Dynamic light scattering optical coherence tomography," *Opt. Express* **20**(20), 22262–22277 (2012).
4. B. K. Huang and M. A. Choma, "Resolving directional ambiguity in dynamic light scattering-based transverse motion velocimetry in optical coherence tomography," *Opt. Lett.* **39**(3), 521–524 (2014).
5. M. A. Choma, A. K. Ellerbee, S. Yordanfar, and J. A. Izatt, "Doppler flow imaging of cytoplasmic streaming using spectral domain phase microscopy," *J. Biomed. Opt.* **11**(2), 024014 (2006).
6. S. Yazdanfar, C. Yang, M. V. Sarunic, and J. A. Izatt, "Frequency estimation precision in Doppler optical coherence tomography using the Cramer-Rao lower bound," *Opt. Express* **13**(2), 410–416 (2005).
7. D. P. Chowdhury, C. M. Sorensen, T. W. Taylor, J. F. Merklin, and T. W. Lester, "Application of photon correlation spectroscopy to flowing brownian motion systems," *Appl. Opt.* **23**(22), 4149–4154 (1984).
8. T. W. Taylor and C. M. Sorensen, "Gaussian beam effects on the photon correlation spectrum from a flowing Brownian motion system," *Appl. Opt.* **25**(14), 2421–2426 (1986).
9. T. G. van Leeuwen, D. J. Faber, and M. C. Aalders, "Measurement of the axial point spread function in scattering media using single-mode fiber-based optical coherence tomography," *IEEE J. Sel. Top. Quantum Electron.* **9**(2), 227–233 (2003).
10. E. Koch, J. Walther, and M. Cuevas, "Limits of Fourier domain Doppler-OCT at high velocities," *Sens. Actuators, A* **156**(1), 8–13 (2009).
11. M. A. Choma, A. K. Ellerbee, C. Yang, T. L. Creazzo, and J. A. Izatt, "Spectral-domain phase microscopy," *Opt. Lett.* **30**(10), 1162–1164 (2005).
12. H. C. Hendargo, R. P. McNabb, A. Dhalla, N. Shepherd, and J. A. Izatt, "Doppler velocity detection limitations in spectrometer-based versus swept-source optical coherence tomography," *Biomed. Opt. Express* **2**(8), 2175–2188 (2011).
13. D. A. Boas, K. K. Bizheva, and A. M. Siegel, "Using dynamic low-coherence interferometry to image Brownian motion within highly scattering media," *Opt. Lett.* **23**(5), 319 (1998).
14. C. S. Kim, W. Qi, J. Zhang, Y. J. Kwon, and Z. Chen, "Imaging and quantifying Brownian motion of micro- and nanoparticles using phase-resolved Doppler variance optical coherence tomography," *J. Biomed. Opt.* **18**(3), 030504 (2013).
15. C. S. Johnson and D. A. Gabriel, *Laser Light Scattering* (Dover Publications, 1994).
16. B. J. Berne and R. Pecora, *Dynamic Light Scattering* (Dover Publications, 2000).
17. N. Uribe-Patarroyo, M. Villiger, and B. E. Bouma, "Quantitative technique for robust and noise-tolerant speed measurements based on speckle decorrelation in optical coherence tomography," *Opt. Express* **22**(20), 24411–24429 (2014).
18. N. Weiss, T. G. van Leeuwen, and J. Kalkman, "Simultaneous and localized measurement of diffusion and flow using optical coherence tomography," *Opt. Express* **23**(3), 3448–3459 (2015).
19. N. Uribe-Patarroyo, A. L. Post, S. Ruiz-Lopera, D. J. Faber, and B. E. Bouma, "Noise and bias in optical coherence tomography intensity signal decorrelation," *OSA Continuum* **3**(4), 709–741 (2020).
20. M. G. O. Gräfe, M. Gondre, and J. F. de Boer, "Precision analysis and optimization in phase decorrelation OCT velocimetry," *Biomed. Opt. Express* **10**(3), 1297–1314 (2019).
21. D. W. Schaefer, "Dynamics of number fluctuations: motile microorganisms," *Science* **180**(4092), 1293–1295 (1973).

22. E. J. Nijman, H. G. Merkus, J. C. M. Marijnissen, and B. Scarlett, "Simulations and experiments on number fluctuations in photon-correlation spectroscopy at low particle concentrations," *Appl. Opt.* **40**(24), 4058–4063 (2001).
23. K. Cheishvili and J. Kalkman, "Scanning dynamic light scattering optical coherence tomography for measurement of high omnidirectional flow velocities," *Opt. Express* **30**(13), 23382–23397 (2022).
24. N. Uribe-Patarroyo and B. E. Bouma, "Velocity gradients in spatially resolved laser Doppler flowmetry and dynamic light scattering with confocal and coherence gating," *Phys. Rev. E* **94**(2), 022604 (2016).
25. R. R. Vardanyan, V. K. Dallakyan, U. Kerst, and C. Boit, "Laser beam transmission and focusing inside media," *J. Contemp. Phys.* **46**(5), 218–225 (2011).
26. A. N. Bashkatov and E. A. Genina, "Water refractive index in dependence on temperature and wavelength: a simple approximation," *Proc. SPIE* **5068**, 393–395 (2003).
27. N. Cheng, "Formula for viscosity of glycerol-water mixture," *Ind. Eng. Chem. Res.* **47**(9), 3285–3288 (2008).
28. H. Bruus, "Acoustofluidics 1: governing equations in microfluidics," *Lab Chip* **11**(22), 3742–3751 (2011).
29. K. Cheishvili, "Number fluctuation DLS-OCT data and analysis routines," Zenodo, 2023, <https://doi.org/10.5281/zenodo.6606471>.